Received: 18 September 2018 | Revised: 21 December 2018 | Accepted: 22 December 2018
DOI: 10.1002/gj.3450

RESEARCH ARTICLE

WILEY

Potassic alkaline granitoid magmatism in the northern margin of the Tarim Craton: First evidence of a back-arc extensional environment

Genwen Chen[1] | Jianxing Yang[1,2] | Rui Liu[3,4]

[1] CAS Key Laboratory of Mineralogy and Metallogeny, Guangzhou Institute of Geochemistry, Chinese Academy of Sciences, Guangzhou, China
[2] University of Chinese Academy of Sciences, Beijing, China
[3] Guangdong Provincial Key Lab of Geodynamics and Geohazards, School of Earth Sciences and Engineering, Sun Yat-sen University, Guangzhou, China
[4] Southern Laboratory of Ocean Science and Engineering (Zhuhai), Guangdong, China

Correspondence
Rui Liu, Guangdong Provincial Key Lab of Geodynamics and Geohazards, School of Earth Sciences and Engineering, Sun Yat-sen University, Guangzhou 510275, China.
Email: liurui35@mail.sysu.edu.cn

Funding information
Deep Resources Exploration and Mining, a Special Project in the Framework of National Key R & D Program of China, Grant/Award Number: 2017YFC0602302; National 305 Project, Grant/Award Number: 2011BAB06B02-03

Handling Editor: G. Yang

The tectonic setting of the northern Tarim Craton during the Palaeozoic is vital to our understanding of the subduction polarity of the paleo-oceanic plates in the Tianshan Orogen and the accretion history of the south-western Central Asian Orogenic Belt. We first identified granitoids intruding the Palaeoproterozoic metamorphic rocks in the Kurchu area in the northern Tarim Craton. The zircon LA-ICP-MS U–Pb dating of this rock indicates that its crystallization age is 418 Ma, highlighting a late Early Palaeozoic magmatic event. Compared with the contemporaneous granitoids in the southern margin of the Tarim Craton, the Kurchu granitoid has high K_2O (6.17–7.25 wt.%) and high alkaline ($Na_2O + K_2O$ = 9.48–10.56 wt.%) contents. The Rittmann index (σ) ranges from 3.53 to 5.68, and samples plot in the shoshonite series in the K_2O–SiO_2 diagram, indicating that the rock is a potassic-alkaline granite (PAG). In addition, this granitoid shows high REE concentrations (264–817 ppm) with significant Eu anomalies and is depleted in Ba, Sr, Nb, Ta, Ti, and P but enriched in Zr and Hf. These geochemical characteristics and high $(^{87}Sr/^{86}Sr)_i$ (0.70857–0.70995) and low $\varepsilon Nd(T)$ (−10.67 to −10.24) values of the Kurchu PAG indicate that this rock was derived from the partial melting of the crust. The diagenetic conditions of the Kurchu PAG are high temperatures, as recorded by higher zircon saturation temperatures (855–919°C), low diagenetic pressure, a less shallow emplacement depth recorded by lower Sr (<200 ppm) concentrations, and a low oxygen fugacity recorded by lower Eu* (0.17–0.89), higher Zr (>355 ppm) and Hf (>9.73 ppm) concentrations, and trace element contents of zircons. In various discrimination diagrams, all samples consistently plot in rift-related areas. These geochemical and diagenetic features suggest that this magmatic event probably occurred in a back-arc environment. Therefore, there is back-arc basin occurring in the northern Tarim Craton in the Early Palaeozoic, which provides strong evidence that this region was an active margin probably much earlier than Silurian, necessitating the southward subduction of the South Tianshan Ocean.

KEYWORDS
back-arc environment, Kurchu, northern Tarim Carton, potassic-alkaline granite

1 | INTRODUCTION

Potassic igneous rocks include a variety of compositions ranging from shoshonites associated with calc-alkaline volcanic rocks to ultrapotassic leucitites (Campbell et al., 2014; Foley & Peccerillo, 1992; Peccerillo, 1992). Potassic igneous rocks have been recognized as an important and integral component of magmatism at destructive continental margins (e.g., Abbasi, Manesh, Karimi, & Parfenova, 2014; Carr, 1998; Costa, Oliveira, & McNaughton, 2011; Ding et al., 2015; Foley & Peccerillo, 1992; Hari, Chalapathi, Vikas, & Guiting, 2014; Liu, Jiang, Jia, Zhao, & Zhou, 2015; Morrison, 1980; Nabatian et al., 2014; Orozco-Garza, Dostal, Keppie, & Paz-Moreno, 2013; Rao, Srivastava, Sinha, & Ravikant, 2014; Rios et al., 2007; Saunders, Tarney, & Weaver, 1980; Torabi, 2011; Yang et al., 2012). Generally, arc-related potassic igneous rocks are younger, stratigraphically higher, and erupted further from the suture than less potassic rocks, although there are exceptions (Arculus & Johnson, 1978). Therefore, potassic igneous rocks can be used to attribute arc-like tectonic affinities to ancient terranes (Barley, Eisenlohr, Groves, Perring, & Vearncombe, 1989; Brooks, Ludden, Pigeon, & Hubregtse, 1982; Wyman & Kerrich, 1989).

The origin of potassic igneous rocks is controversial (Peccerillo, 1992). Generally, in a subduction system, these rocks are derived from the partial melting of mantle that is metasomatically modified by subduction-related fluids (Aoki, Ishiwaka, & Kanisawa, 1981; Edgar & Arima, 1985; Foley & Peccerillo, 1992; Jiang et al., 2015; Morrison, 1980; Peccerillo, 1992), subducted oceanic crust (Shen, Shen, Liu, Li, & Zeng, 2008), subducted marine sediment (Liu et al., 2014; Mallik, Nelson, & Dasgupta, 2015; Miller, Schuster, Klötzli, Frank, & Purtscheller, 1999; Rogers, Hawkesworth, Parker, & Marsh, 1985; Woodhead, Hergt, Davidson, & Eggins, 2001), and the overlying mantle wedge (Bucholz, Jagoutz, Schmidt, & Sambuu, 2014; Ellam & Hawkesworth, 1988). The metasomatic hypothesis for the origin of shoshonites is consistent with the experimental work of Wyllie and Sekine (1982), who showed that potassic magmas can be produced by melting the hydrated mantle. On the other hand, post-collisional potassic igneous rock from the East African Orogen (Küster & Harms, 1998) and the Kunlun Orogenic Belt, Xinjiang (Jiang et al., 2002), are quartz-saturated and therefore cannot be derived directly from the mantle. It has been suggested that these rocks were derived from the partial melting of the lower crust following underplating by mantle-derived magma (Jiang et al., 2002; Küster & Harms, 1998). Therefore, the origin of potassic igneous rock is related to the geological setting where these rocks occur.

The Tianshan Orogen occupies the south-western Central Asian Orogenic Belt (CAOB; Figure 1a), which played a major role in the assembly of Eurasia and is also known for its role in large-scale Phanerozoic continental growth by adding juvenile materials from the depleted mantle (e.g., Jahn, 2004). It was created during the Palaeozoic by the subduction and accretionary orogeny of several intervening ancient oceans located between the Tarim Craton, Central Tianshan Block (CTB), Kazakhstan–Yili Block (KYB), and Jungger Block (e.g., Allen, Windley, & Zhang, 1993; Charvet et al., 2011; Gao et al., 2012; Gao, Li, Xiao, Tang, & He, 1998; Wang et al., 2010; Windley, Allen, Zhang, Zhao, & Wang, 1990; Xiao et al., 2009; Xiao, Zhang, Qin, Sun, & Li, 2004; Zhu, Charvet, Xiao, & Jahn, 2011; Figure 1b). The Tianshan Orogen is a key area for understanding the final accretion of the CAOB (e.g., Xiao et al., 2004; Xiao et al., 2009). However, the tectonic evolution of the Tianshan Orogen is still controversial, especially in terms of the subduction polarity of the South Tianshan Ocean. Based on the widespread occurrence of Palaeozoic arc magmatism in the KYB and the CTB and the presence of HP–UHP metamorphic rocks along the northern margin of the South Tianshan accretionary complex, some researchers (e.g., Allen et al., 1993; Gao et al., 1998; Gao et al., 2012; Gao & Klemd, 2003; Windley et al., 1990; Xiao et al., 2004; Xiao et al., 2009) proposed that the South Tianshan Ocean subducted northward (present coordinates) under the CTB, thus indicating that the northern Tarim Craton was a passive continental margin and no tectonic accretion or crustal growth occurred (Ge et al., 2012). Other researchers (e.g., Charvet et al., 2011; Lin, Faure, Shi, Wang, & Li, 2009; Wang et al., 2010) proposed a southward subduction model based on the north-verging ductile deformation observed in the accretionary complexes. In addition, in recent years, many researchers have argued for a late Early Palaeozoic continental arc setting for the rocks in the northern margin of the Tarim Craton and provided much magmatic evidence for the

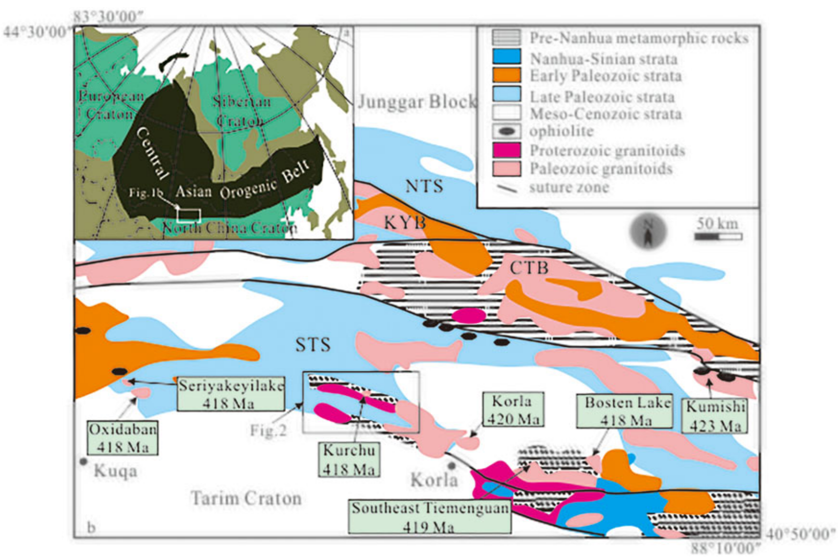

FIGURE 1 (a) Topography and tectonic units in Asia. (b) Geological map of the Tianshan Orogen simplified from XBGMR (1993); NTS: Northern Tianshan; KYB: Kazakhstan–Yili Block; CTB: Central Tianshan Block; STS: Southern Tianshan. The granitic ages in (b) are from Ge et al. (2012), Guo et al. (2013), Zhang, Zhou, Li, and Wang (2007), Zhang et al. (2014), and Zhu et al. (2008) [Colour figure can be viewed at wileyonlinelibrary.com]

southward subduction model (Ge et al., 2012; Guo et al., 2013; Zhang et al., 2014; Zhang, Zhou, Wang, & Wang, 2007; Zhu et al., 2008). However, until now, there has been a lack of evidence for a back-arc setting in the northern margin of the Tarim Craton on which to structure an entire subduction system. Therefore, here, we focus on the northern margin of the Tarim Craton to study the subduction polarity of the ancient oceanic plates in the Tianshan Orogen during the Palaeozoic.

In this contribution, we report the zircon U–Pb ages and Sr–Nd isotopic and whole-rock geochemical data of potassic granitoids intruding into the Precambrian basement of the Tarim Craton in the Korla area. Our data first argue for a late Early Palaeozoic back-arc setting for these rocks, which is first found in the northern margin of the Tarim Craton. Thus, we not only provide strong magmatic evidence for the southward subduction model but also demonstrate the existence of an entire subduction system. In addition, we describe the origin of potassic granitoids occurring in the subduction system, proving that the potassic granitoids in a subduction system can also be derived from the partial melting of the lower crust.

2 | GEOLOGICAL SETTING

The Tarim Craton, which is located in the south of the CAOB and has an area of more than 600,000 km^2, is one of the oldest cratons in China (Lu, Li, Zhang, & Niu, 2008). The subduction and accretionary orogeny of intervening ancient ocean plates located between the Tarim Craton and Central Tianshan Block created the Southern Tianshan. The Southern Tianshan is separated from the Tarim Craton by the North Tarim Thrust (Ge et al., 2012). (Meta)sediments in this region include Mesoproterozoic to Early Neoproterozoic marine sequences, Late Neoproterozoic sedimentary cover, and Palaeozoic marine sequences. In addition, extensive granitoids also occur in this area (Figure 1b). Granitoids, which occur as plutons, dykes, or stocks ranging from tens of metres to several kilometres in width, include Mesoproterozoic, Neoproterozoic, and Early Palaeozoic granitoids, which all intrude the Neoarchean strata and are covered by Palaeozoic strata. The Kurchu area is located to the south of the North Tarim Thrust (Figure 1b). The oldest strata in this area are the Neoarchean gneiss and schist, which consist of biotite plagioclase gneiss, biotite amphibolite plagioclase gneiss, sericite-quartz schist, and two-mica feldspar schist (Figure 1b). Palaeozoic strata, which are widely exposed in the Kurchu area, include the late Devonian strata in the north and the Carboniferous strata in the middle. The late Devonian strata mainly consist of tuffaceous sandstone and marble, and the Carboniferous strata are dominated by marine carbonate and clastic sequences (Figure 2).

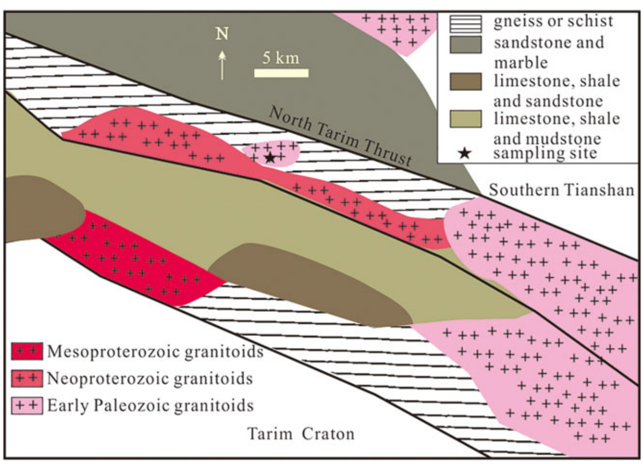

FIGURE 2 Geological map of the Korla area, modified after XBGMR (1993) [Colour figure can be viewed at wileyonlinelibrary.com]

Previous studies indicate that granitoids formed at the Early Palaeozoic (418–423 Ma) in this region have different characteristics and genesis. Some plutons were derived from the partial melting of the Palaeoproterozoic continental crust with inputs from juvenile depleted mantle materials (Ge et al., 2012; Guo et al., 2013), such as the Tiereke, Kurla, and Tiemenguan plutons. Some plutons were generated by the partial melting of high-K meta-basalt (Guo et al., 2013), such as the Oxidaban and Bositen Lake plutons. In addition, the Kumishen pluton was formed by the partial melting of Mesoproterozoic mantle-derived basic materials (Zhang et al., 2007).

In this study, we report the systematic zircon U–Pb geochronology, Sr–Nd isotopes, and geochemistry compositions of the granitoids that are well exposed in the middle of the Kurchu area. The outcrops of these granitoids occur as plutons that are 1 km in width and 2.5 km in length.

3 | PETROGRAPHY

Field and thin-section observations suggest that these rocks are syenogranite. The rocks mainly exhibit granitic texture. They are mainly composed of platy plagioclase (20 vol.%), anhedral orthoclase (40 vol.%), and microcline (20 vol.%) as well as minor quartz (Figure 3). The accessory minerals consist of zircon and apatite. The plagioclase, orthoclase, and microcline obviously exhibit corrosion structure (Figure 3a) and reaction rim texture (Figure 3b), which indicates that these minerals are magmatic genesis. The hydrous minerals are uncommon in these rocks, indicating that the water content of these rocks is low.

4 | METHODS

4.1 | Zircon U–Pb dating and trace elements

The LA-ICP-MS method was used for zircon U–Pb dating. Zircon separation was carried out using conventional density and magnetic separation techniques to concentrate the non-magnetic heavy fractions; they were then mounted in epoxy under a binocular microscope and polished to expose the cores of the grains. All mounted zircon grains were studied petrographically via transmitted and reflected light microscopy, as well as by cathodoluminescence (CL) imaging to reveal their internal structures. CL imaging was performed using a JEOLJXA-8100 Superprobe at the Guangzhou Institute of Geochemistry, Chinese Academy of Sciences (GIG CAS). Most grains are transparent euhedral crystals ranging in size from 50 to 100 mm. Zircon U–Pb

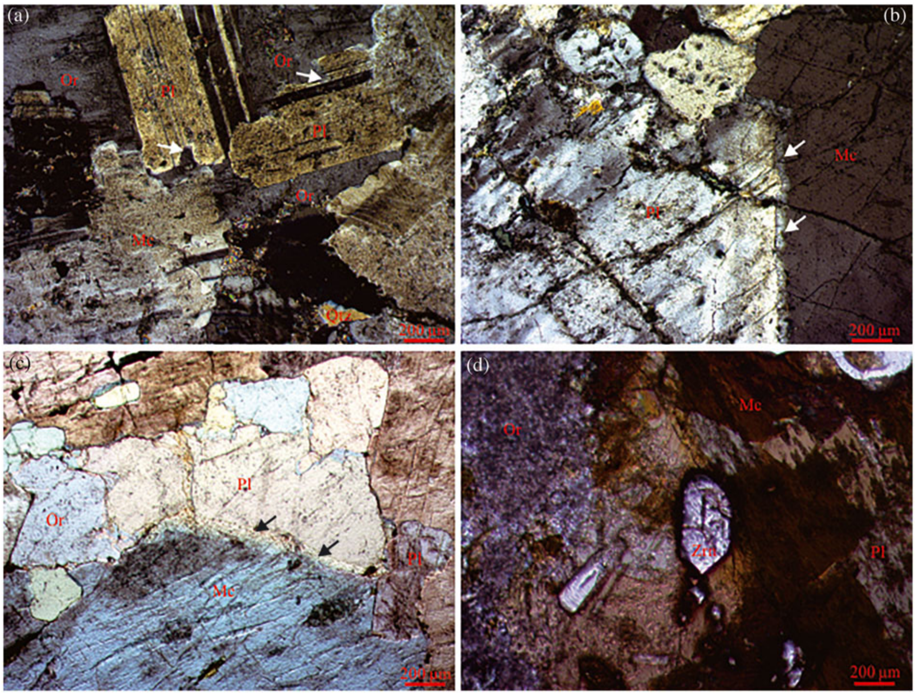

FIGURE 3 Microphotographs (cross-polarized light) of the Kurchu potassic alkaline granitoids (PAG), showing (a) corrosion structure (white arrow) and reaction rim texture (white arrow in b and black arrow in c). (d) Accessory minerals in the Kurchu PAG. Mc: microcline; Or: orthoclase; Pl: plagioclase; Qtz: quartz; Zrn: zircon [Colour figure can be viewed at wileyonlinelibrary.com]

dating and trace elements were conducted at the GIG CAS, using an Agilent 7500a ICP-MS equipped with a 193-nm laser with a repetition rate of 8 Hz and a spot diameter of 31 μm. The zircon Temora standard was used for external standardization, and the Qinghu standard and NIST SRM 610 glass were used to optimize the machine. The operating conditions for the laser ablation system and the ICP-MS instrument, as well as the data reduction techniques, follow the methods of Li et al. (2012). The results are plotted using Isoplot2.0 (Ludwig, 2000).

4.2 | Whole-rock major and trace elements

All samples were crushed into powders of less than 200 mesh in size in an agate shatterbox. The geochemical analyses of major and minor elements were undertaken at the GIG CAS. Major oxide concentrations were measured by XRF spectrometry with an analytical precision of better than ±0.01%. Trace element contents were determined at the GIG CAS using inductively coupled plasma mass spectrometry (ICP-MS). The analytical precisions are better than ±5% for trace elements.

4.3 | Whole-rock Sr–Nd isotope

Sr and Nd isotopes were determined using an ISOPROBE-T thermal ionization mass spectrometer at the Beijing Research Institute of Uranium Geology. Powdered samples were dissolved in Savillex bombs by following a series of standard procedures until the samples were completely dissolved. The isolation of Sr and Nd was achieved using a 2-column technique; Sr fractions were occasionally further purified using a third column. $^{143}Nd/^{144}Nd$ ratios were normalized to a value of $^{146}Nd/^{144}Nd = 0.7219$, whereas $^{87}Sr/^{86}Sr$ ratios were normalized to $^{86}Sr/^{88}Sr = 0.1194$. All $^{87}Sr/^{86}Sr$ ratios reported herein have been duly adjusted to NBS-987 = 0.710250 ± 7. The internal correction for the Sr isotope was $^{86}Sr/^{88}Sr = 0.1194$. The measurement result of standard (NBS987) is 0.710250 ± 7. The $^{143}Nd/^{144}Nd$ ratios were corrected using a value of $^{146}Nd/^{144}Nd = 0.7219$. Our measurements of the SHINESTU Nd standard yielded a value of 0.512118 ± 3.

5 | RESULTS

5.1 | Zircon U–Pb isotopic systematics and trace elements

The zircon grains from the Kurchu granitoids are generally transparent, euhedral, or subhedral, with length to width ratios ranging from 1:1.5 to 1:3, and they contain oscillatory magmatic zoning indicative of magmatic genesis (Figure 4). A total of 16 analyses of zircon grains in the Kurchu granitoids were undertaken. All analyses yielded concordant $^{206}Pb/^{238}U$ ages ranging from 406.5 to 436.4 Ma (Table 1) and a weighted mean $^{206}Pb/^{238}U$ age of 421.8 ± 5.6 Ma (2σ; n = 14) with an MSWD value of 3.7 (Figure 5).

The zircon grains from the Kurchu PAG have enriched HREE relative to LREE, similar to the patterns of magmatic zircon grains in igneous rocks (Hoskin & Schaltegger, 2003). The Ti-in-zircon temperature varies from 772°C to 838°C (average 794°C, n = 14; Table 2).

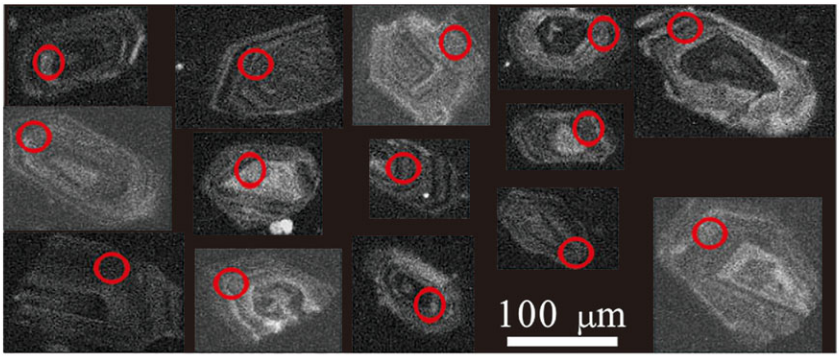

FIGURE 4 Typical CL images of zircons for the three samples from the studied PAG [Colour figure can be viewed at wileyonlinelibrary.com]

TABLE 1 Zircon U–Pb dating results of the Kurchu PAG

Samples	Th (ppm)	U (ppm)	Th/U	Isotopic ratios $^{207}Pb/^{206}Pb$	1σ	$^{207}Pb/^{235}U$	1σ	$^{206}Pb/^{238}U$	1σ	Apparent ages (Ma) $^{207}Pb/^{206}Pb$	1σ	$^{207}Pb/^{235}U$	1σ	$^{206}Pb/^{238}U$	1σ
KRC01-01	1343.73	354.17	3.79	0.5494	0.0664	0.5101	0.0337	0.0674	0.0012	4380	166	419	23	421	7
KRC01-02	470.50	177.14	2.66	0.58011	0.0607	0.5478	0.0158	0.0686	0.0008	4459	144	444	10	427	5
KRC01-03	305.18	254.15	1.20	0.55941	0.0594	0.5270	0.0176	0.0684	0.0008	4406	147	430	12	427	5
KRC01-04	197.49	74.83	2.64	0.73192	0.0767	0.6911	0.0193	0.0686	0.0008	4795	142	534	12	427	5
KRC01-05	119.16	135.67	0.88	0.58775	0.0623	0.5357	0.0158	0.0662	0.0008	4478	146	436	10	413	5
KRC01-06	1228.26	342.75	3.58	0.58594	0.0623	0.5270	0.0157	0.0653	0.0008	4474	146	430	10	408	5
KRC01-07	4371.92	709.93	6.16	0.58982	0.0664	0.5329	0.0248	0.0656	0.0010	4483	155	434	16	409	6
KRC01-08	192.34	134.13	1.43	0.56118	0.0599	0.5263	0.0161	0.0681	0.0008	4411	148	429	11	425	5
KRC01-09	270.91	235.32	1.15	0.82044	0.0908	0.7753	0.0302	0.0686	0.0010	4958	149	583	17	428	6
KRC01-10	62.60	69.02	0.91	0.63136	0.0681	0.6096	0.0184	0.0701	0.0008	4582	148	483	12	436	5
KRC01-11	5084.90	858.43	5.92	0.65132	0.0697	0.6179	0.0166	0.0688	0.0008	4627	146	489	10	429	5
KRC01-12	1343.73	354.17	3.79	0.58906	0.0638	0.5286	0.0149	0.0651	0.0007	4481	149	431	10	407	4
KRC01-13	470.50	177.14	2.66	0.64067	0.0787	0.6131	0.0386	0.0694	0.0012	4603	167	486	24	433	7
KRC01-14	305.18	254.15	1.20	0.71261	0.0770	0.6694	0.0172	0.0681	0.0008	4756	147	520	10	425	5

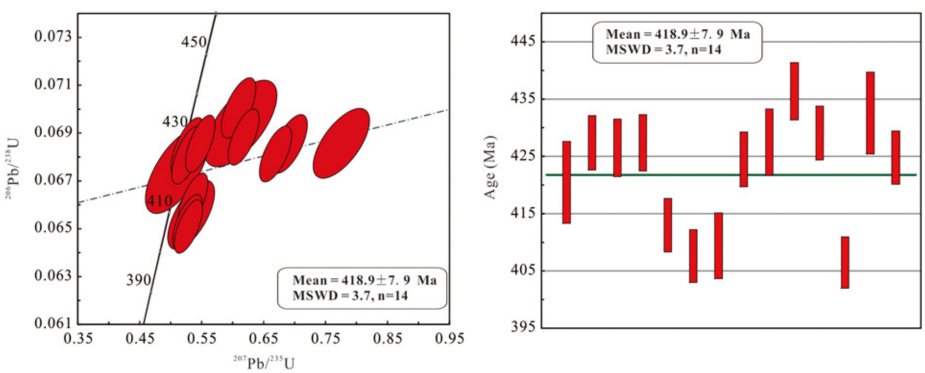

FIGURE 5 U–Pb concordia and weighted average ages for the 14 zircons from the studied PAG [Colour figure can be viewed at wileyonlinelibrary.com]

TABLE 2 Major (wt.%) and trace elements (ppm) of zircons in the Kurchu PAG

Samples	KRG01-01	KRG01-02	KRG01-03	KRG01-04	KRG01-05	KRG01-06	KRG01-07	KRG01-08	KRG01-09	KRG01-10	KRG01-11	KRG01-12	KRG01-13	KRG01-14
ZrO_2	49.61	52.52	53.61	55.19	50.86	50.46	50.73	56.20	52.78	53.57	51.25	53.98	52.72	50.83
Ti	32.76	3.18	4.16	3.40	5.19	16.66	15.07	4.54	3.24	15.79	14.15	4.44	33.76	9.61
Y	1791.78	1442.74	1117.05	421.12	1038.16	1565.33	2512.75	1099.65	1540.00	358.03	3523.24	897.01	3197.42	931.89
Nb	6.82	1.77	0.67	0.95	0.20	6.23	32.88	0.82	0.42	0.65	38.89	0.19	27.46	4.35
La	0.01	0.00	0.00	0.00	0.01	0.04	0.02	0.00	0.02	0.00	0.04	0.03	0.17	0.00
Ce	6.60	3.59	5.94	1.19	2.40	7.04	15.18	2.42	4.26	9.26	20.05	2.68	17.97	2.55
Pr	0.06	0.01	0.05	0.00	0.02	0.05	0.08	0.03	0.03	0.03	0.10	0.00	0.15	0.02
Nd	1.10	0.16	0.54	0.05	0.37	0.79	1.52	0.28	0.55	0.53	2.13	0.15	1.90	0.03
Sm	2.30	1.13	1.13	0.52	0.81	2.40	4.37	1.18	1.63	1.15	5.54	0.55	4.40	0.75
Eu	1.11	0.56	1.05	0.13	0.80	1.13	1.77	0.63	1.27	0.33	2.21	0.57	2.02	0.37
Gd	19.46	12.87	11.11	3.49	9.74	18.76	34.34	10.72	15.07	6.98	46.02	6.34	35.29	7.59
Tb	7.36	5.66	4.23	1.59	3.81	7.52	12.99	4.60	6.10	2.21	17.96	2.88	14.47	3.27
Dy	103.11	86.13	61.40	25.03	57.23	100.26	173.03	66.50	88.70	27.63	236.88	45.76	194.99	51.33
Ho	46.17	40.22	31.11	12.06	28.73	43.58	71.81	31.26	43.00	11.33	99.54	24.54	83.36	24.56
Er	231.49	211.82	170.99	66.40	163.63	219.97	343.48	169.08	235.86	55.10	475.20	147.44	411.77	132.45
Tm	53.62	52.23	43.10	16.75	41.47	51.72	77.45	41.96	59.49	12.42	107.45	38.21	93.98	32.89
Yb	546.01	565.84	499.59	188.10	495.67	545.94	770.11	464.92	684.77	129.11	1063.79	465.45	957.90	366.86
Lu	127.10	143.18	145.76	48.55	142.98	135.16	166.32	120.42	190.37	28.45	232.79	137.22	210.17	88.08
Hf	8760.77	9457.22	8442.24	6275.12	7799.36	8426.11	9641.91	7850.54	8496.69	8888.43	11578.49	8554.31	10393.87	7812.90
Ta	0.52	0.19	0.03	0.08	0.03	0.45	2.99	0.13	0.04	0.31	3.91	0.01	1.81	0.42
Th	1343.73	470.50	305.18	197.49	119.16	1228.26	4371.92	192.34	270.91	62.60	5084.90	79.23	3799.31	592.23
T_{Ti}	857	635	675	687	788	778	676	830	651	773	765	678	674	861
log (fO_2)	−6.75	−18.62	−17.34	−17.74	−12.30	−9.93	−10.09	−21.34	−19.16	−10.38	−16.47	−22.88	−16.58	−10.42

5.2 | Whole-rock compositions

Major and trace element compositions were determined for eight samples collected from the Kurchu granitoids. In Table 3, the chemical compositions of all eight samples are reported. The granitoids contain low SiO_2 (61.8–69.6 wt.%), MgO (0.24–1.08 wt.%), and CaO (0.89–1.84 wt.%) contents and are highly enriched in Al_2O_3 (14.85–17.63 wt.%), K_2O (6.17–7.25 wt.%), and alkalis ($Na_2O + K_2O$: 9.48–10.56 wt.%). Their K_2O/Na_2O ratios range from 1.58 to 2.29. The Rittmann index (σ) ranges from 3.53 to 5.68, and the samples plot in

TABLE 3 Major (wt.%) and trace elements (ppm) of the Kurchu PAG

Samples	KRC01	KRC02	KRC03	KRC04	KRC05	KRC06	KRC07	KRC08
SiO_2	67.1	61.77	64.51	68.08	68.03	63	65.84	69.57
Al_2O_3	15.83	17.07	15.76	14.85	16.21	17.63	16.27	15.33
Fe_2O_3	0.69	0.72	0.51	0.08	2.85	4.05	3.67	2.91
FeOt	2.01	3.01	2.91	2.61	2.57	3.65	3.30	2.62
MgO	0.32	0.91	0.46	0.24	0.32	1.08	0.48	0.27
CaO	0.89	1.75	1.04	1.12	0.92	1.84	1.08	1.19
Na_2O	3.88	3.13	3.51	3.27	4.05	3.31	3.74	3.51
K_2O	6.39	7.19	6.55	6.21	6.39	7.25	6.68	6.17
MnO	0.02	0.06	0.05	0.05	0.02	0.06	0.05	0.05
P_2O_5	0.03	0.12	0.07	0.04	0.03	0.13	0.07	0.04
TiO_2	0.27	0.58	0.41	0.3	0.26	0.62	0.42	0.29
LOI	0.46	0.68	1.17	0.43	0.57	0.85	1.34	0.55
Total	99.86	99.93	99.85	99.86	99.68	99.95	99.74	99.94
σ	4.37	5.68	4.71	3.58	4.35	5.58	4.75	3.53
A.R	2.73	2	2.44	2.38	2.79	2.03	2.52	2.48
$K_2O/N_{a2}O$	1.65	2.29	1.87	1.9	1.58	2.19	1.79	1.76
Ba	211.39	987.65	690.74	328.38	186.5	872	632	295
Co	27.5	28.74	32.15	45.14	25.3	27	29.6	41.6
Ga	23.99	21.58	20.93	22.54	23.2	21	20.7	22
Hf	12.38	18.23	12.9	9.73	15.1	17.5	15.6	12.5
Nb	31.25	21.84	28.53	26.29	21.1	14.9	19.3	17.5
Pb	25.3	28.1	24.13	29.27	22	25	22	25
Rb	152	151.8	138.3	130.9	135.5	143.5	135.5	133.5
Sr	72.5	199.7	114.6	60.8	65	199	115	58
Ta	1.46	1.62	1.82	1.42	1.2	1.3	1.5	1.2
Th	32.51	12.21	24.13	24.89	37.5	12.3	27	25.7
U	2.11	1.67	1.95	1.73	2.46	1.54	2.29	1.81
Zn	30.63	58.53	50.61	55.28	25	53	46	49
Zr	464.1	651.2	504.1	355.3	528	769	605	433
La	217.74	63.2	153.26	114.85	168.5	63.2	126.5	96.3
Ce	377.86	116.3	273.75	209.71	317	117	237	192.5
Pr	40.49	13.17	29.5	23.11	33.1	12.55	25	20.7
Nd	132.1	46.68	99.32	79.36	115	46.4	88.8	74.8
Sm	17.35	6.61	14.05	12.02	15.1	6.74	12.6	11.55
Eu	0.74	1.66	1.36	0.66	0.61	1.56	1.19	0.58
Gd	10.89	4.92	9.81	8.55	12.5	5.86	11.2	9.55
Tb	1.55	0.77	1.48	1.27	1.41	0.76	1.34	1.18
Dy	8.32	4.33	7.96	6.72	6.44	3.97	6.71	5.87
Ho	1.52	0.85	1.49	1.26	1.24	0.8	1.28	1.12
Er	3.98	2.34	3.72	3.18	3.63	2.37	3.66	3.11
Tm	0.58	0.35	0.56	0.49	0.5	0.36	0.52	0.45
Yb	3.91	2.44	3.54	3.09	2.93	2.17	3.03	2.53
Lu	0.56	0.36	0.52	0.45	0.46	0.34	0.48	0.4
Y	36.08	20.82	34.33	29.37	31.2	20.9	31.3	26.9
∑REE	817.6	264.0	600.3	464.7	678.4	264.1	519.3	420.6
Eu/Eu*	0.17	0.89	0.35	0.20	0.14	0.76	0.31	0.17

the shoshonite series in the K_2O–SiO_2 diagram (Figure 6a), indicating that the rock is potassic-alkaline granite (PAG). On the Q–A–P diagram, these samples mostly plot in the quartz-syenite area (Figure 6 b), which is consistent with field and thin-section observations. Their A/NK and A/CNK (1.02 to 1.33) values indicate that they are weakly peraluminous granitoids (Figure 7).

These samples yield high total rare earth element concentrations (ΣREE = 264–817 ppm; Table 3). The concentrations of LREE are high, and on the chondrite-normalized diagram, LREE are highly enriched relative to HREE (La_N/Yb_N = 17.4–38.8), thus showing relatively flattened distribution patterns. A significant Eu anomaly was observed in these samples (Eu* = 0.17–0.89; Figure 8a). The primordial mantle-normalized spider diagram shows that these samples are relatively depleted in high-field-strength elements, for example, Nb, Ta, and Ti. In addition, Ba, Sr, and P are highly depleted (Figure 8b). The concentrations of Zr, Hf, and Yb are high, but the concentration of Sr is low.

5.3 | Sm/Nd and Rb/Sr isotope data

Four granitoid samples were selected for the determination of their $^{143}Nd/^{144}Nd$ and $^{87}Sr/^{86}Sr$ ratios. The analysed Nd and Sr isotope contents of the samples and initial $^{143}Nd/^{144}Nd$, $^{147}Sm/^{144}Nd$, $^{87}Sr/^{86}Sr$, and $^{87}Rb/^{86}Sr$ ratios and εNd(*T*) are presented in Table 4. The initial ratios were calculated based on 418 Ma according to the U–Pb age of the granitoid samples. The initial $^{87}Sr/^{86}Sr$ ratios of the granitoids range from 0.70857 to 0.70995 (the KRC02 is 0.70011). The initial $^{143}Nd/^{144}Nd$ values range from 0.51155 to 0.51157. The εNd(*T*) values of the granitoids also range from −10.24 to −10.67. Nd model ages (T_{DM}) were calculated via a two-stage model for the granitoids. The data in Table 4 show that the T_{DM2} values range from1994 to 2028 Ma.

6 | DISCUSSION

6.1 | The diagenetic conditions of the Kurchu potassic-alkaline granitoids (PAG)

Previous studies indicated that the fluid phase only occurs at depths of thousands of metres under the Earth (Chen, Chen, Zaw, Pirajno, & Zhang, 2004; Yardley & Valley, 1997). Therefore, the partial melting of crust is the main genesis of magma formation within the crust (Clemens & Vielzeuf, 1987). Thus, the composition of magma is affected not only by the composition of the source (Patiňo-Douce & McCarty, 1998; Roberts, 1993) but also by the diagenetic conditions, including temperature, pressure, and oxidized fugacity (Patiňo-Douce & McCarty, 1998).

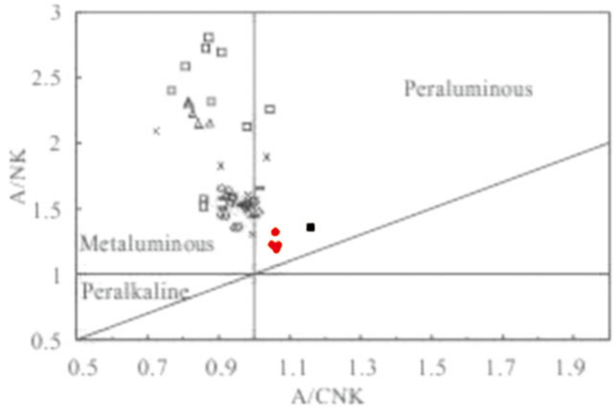

FIGURE 7 A/CNK–A/NK diagram for the studied PAG, after Shand (1943). The legend is the same as that in Figure 6 [Colour figure can be viewed at wileyonlinelibrary.com]

The relatively high temperature of crystallization, approximately 855°C to 919°C, of the Kurchu PAG is indicated by the saturation of zircon (Watson & Harrison, 1983) in a bivariate plot of whole-rock Zr (ppm) versus the cation ratio M = (Na + K + 2Ca)/(Al × Si) (Figure 9a). The Kurchu PAG has higher Zr and Hf concentrations (Figure 9b). The behaviours of Zr and Hf are controlled by water content (Baker, Conte, Freda, & Ottolini, 2002). These elements are immobile in fluid-dominated systems, and they remain in a solid phase during partial melting (Richards, 2005). Therefore, the greater the water content of a magma is, the lower the Zr and Hf concentrations in the magma are. Consequently, the relatively high Zr and Hf abundances of the Kurchu PAG suggest relatively low water concentrations. On the other hand, the common occurrence of plagioclase and minor biotite also indicates the presence of little H_2O in the system. In the system Q–Ab–Or–H_2O–CO_2 at 2 kbar and H_2O = 2.1 wt.% projected on to the fluid-free base Q-Ab-Or (after Holtz, 1992), the granites largely plot between 870°C to 910°C (Figure 10a). These results are in accordance with the inferred zircon saturation

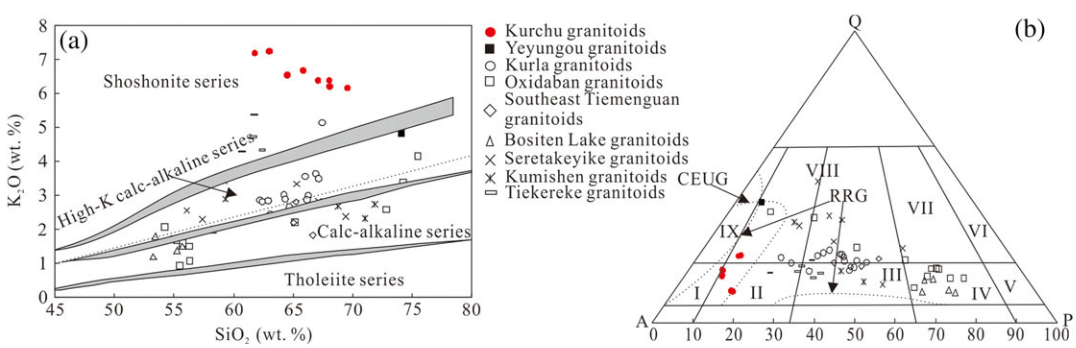

FIGURE 6 Classification diagrams for the studied PAG. (a) SiO_2–K_2O, after Peccerillo and Taylor (1976); (b) Q–A–P diagram, after Maniar and Piccoli (1989). RRG: rift-related granitoids, CEUG: continental epeirogenic uplift granitoids. The granitic geochemical data are from Ge et al. (2012), Guo et al. (2013), Han, He, and Wu (2004), Wang et al. (2009), Zhang et al. (2007), Zhang et al. (2014), and Zhu et al. (2008) [Colour figure can be viewed at wileyonlinelibrary.com]

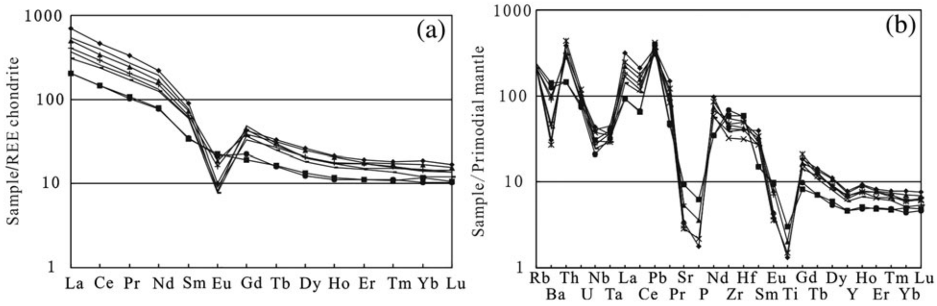

FIGURE 8 (a) Chondrite-normalized REE pattern and (b) primitive mantle-normalized trace element spider diagram of the studied granodiorite. Average chondrite- and primitive mantle-normalizing values are from Sun and McDonough (1989)

TABLE 4 Sr–Nd isotope data of the Kurchu PAG

Samples	Rb (ppm)	Sr (ppm)	$^{87}Rb/^{86}Sr$	$^{87}Sr/^{86}Sr$	I_{Sr}	Sm (ppm)	Nd (ppm)	$^{147}Sm/^{144}Nd$	$^{143}Nd/^{144}Nd$	εNd(*T*)	$T_{DM,2}$(Ma)
KRC01	152	72.5	6.08825	0.74508	0.70883	17.35	132.1	0.07939	0.51179	−10.29	1994
KRC02	151.8	119.7	3.67445	0.72214	0.70027	6.61	46.68	0.08559	0.51180	−10.37	2000
KRC03	138.3	114.6	3.49949	0.73046	0.70962	14.05	99.32	0.08550	0.51179	−10.71	2028
KRC04	130.9	60.8	6.25349	0.74744	0.71021	12.02	79.36	0.09155	0.51182	−10.33	1997

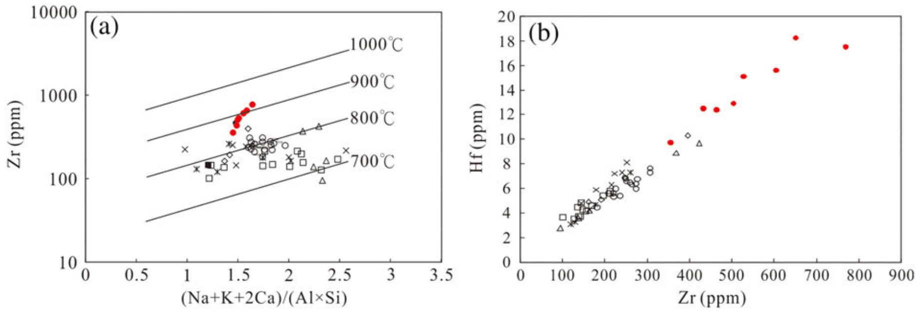

FIGURE 9 (a) Zircon saturation temperature and (b) Zr–Hf diagrams for the studied PAG. The legend is the same as that in Figure 6 [Colour figure can be viewed at wileyonlinelibrary.com]

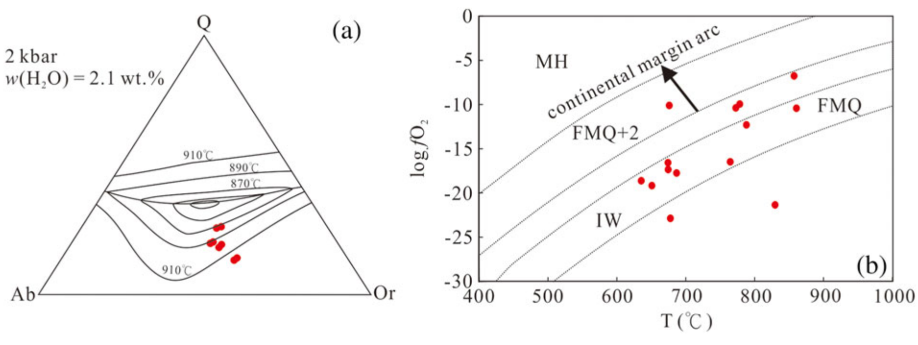

FIGURE 10 (a) Q–Ab–Or diagram, after Holtz (1992) and (b) T (Ti-in-zircon thermometer)–logfO_2 of zircon diagram. The legend is the same as that in Figure 5 [Colour figure can be viewed at wileyonlinelibrary.com]

temperatures of 850°C to 900°C, indicating the derivation of these granitoids at a low water concentration with $w(H_2O)$ = 2.1 wt.%. In addition, Eu^{2+} has the same charge and a similar radius as Ca^{2+}, and it can thus readily substitute for Ca^{2+} in Ca-bearing minerals. Thus, the relative concentration of Eu in a fluid or magma is a function of redox conditions (or the water content; Sverjensky, 1984; Wood, Bryndzia, & Johnson, 1990). Magma will be depleted of Eu in reducing conditions (low fO_2 or low water content) with the fractional crystallization of calcic plagioclase in the magma source (Whitney, 1975). Consequently, the characteristic Eu data in these rocks indicate that they have low fO_2 and/or low water content. These characteristics of the ore system are consistent with the fO_2 data recorded by zircons. Zircon can be used to determine the magmatic oxidation state, as it is a widespread accessory mineral in intermediate to felsic igneous rocks and is resistant to hydrothermal alteration and physical and chemical weathering. In the T (Ti-in-zircon thermometer) versus logfO_2 of zircon chart, most samples plot below the fayalite-magnetite-quartz (FMQ) + 2 buffer curve (Figure 10b), which is the oxygen buffer of granitoids that form in an arc setting (Sun et al., 2015). In addition, the behaviours of Sr and Yb are closely related to the residual phase, which has a different mineral assemblage at different pressures. Therefore, the concentrations of Sr and Yb in granitoids can reflect the pressure of their sources. As mentioned above, plagioclase could have been present and amphibole and garnet absent in the residual source of the studied rocks. Plagioclase being present as a residual phase in the source commonly occurs at low pressure and shallow depths, and amphibole and garnet being present as the residual phases in sources commonly occurs at high pressure and deep depths. Therefore, the Kurchu PAG, which has low Sr and high Yb contents, may have been generated at low pressure and emplaced at shallow depths. Overall, the zircon saturation temperature of the granitoids, their Yb, Zr, and Hf abundances, their depletion of Sr and Eu, and their normative Q–Ab–Or values suggest that these rocks were generated at high temperatures and emplaced at shallow depths from a magma that was relatively anhydrous and reduced in nature (Frost et al., 2001).

Compared with the contemporaneous granitoids in the southern margin of the Tarim Craton, the Kurchu PAG has a higher diagenetic temperature recorded by the zircon saturation temperature, lower diagenetic pressure, and less shallow emplacement depth indicated by its Sr and Yb concentrations and lower oxygen fugacity conditions indicated by its Eu, Zr, and Hf concentrations.

6.2 | The origin of the Kurchu potassic-alkaline granitoids (PAG)

According to previous studies, extensive Early Palaeozoic granitoids occur in the southern margin of the Tarim Craton (Figure 1b), such as the Tiekereke, Seriyakeyilake, Oxidaban, Kurchu, Korla, Southeast Tiemenguan, Bosten Lake, and Kumishi plutons. However, in this study, we first find that the Kurchu PAGs have unique geochemical characteristics, which are significantly different from those of the other Early Palaeozoic granitoids in this area. The Kurchu PAGs have lower MgO and Mg# than other granitoids in this area (Figure 11a). However, their concentrations of K_2O and alkaline (K_2O + Na_2O) are much higher than those of other granitoids. In the Q–A–P diagram, the Kurchu PAGs plot as syenite, but the other plot as diorite, granodiorite, and granite (Figure 6b). In addition, compared with other Early Palaeozoic granitoids in the southern margin of the Tarim Craton, the Kurchu PAGs have higher Zr, Hf, and REE contents and lower Sr contents (Figures 9b and 11b). The zircon saturation temperatures (T_{Zr}) of the Kurchu PAGs are also higher than those of the other granitoids in this area (Figure 9a). The $(^{87}Sr/^{86}Sr)_i$ values of the Kurchu PAGs are higher, but their $\varepsilon_{Nd}(t)$ values are lower, than those of the other granitoids (Figure 12). All of these differences indicate that the Kurchu PAGs are unique in this area.

Generally, related petrologic experiments have proved that the partial melting of mantle cannot directly generate granitic rocks and can only generate basaltic or basaltic-andesitic magmas. In addition, the fractional crystallization of basaltic magma can only generate minor volumes of granite (≈5%). If the Kurchu PAGs were derived from the extensive fractionation of mantle melts, then the volume of mafic magma intruding into the crust may be an order of magnitude greater than that of syenite due to its high degree of fractionation (Frost, Frost, Bell, & Chamberlain, 2002; Turner, Foden, & Morrison, 1992). However, field evidence indicates that the Kurchu PAGs are not directly associated with either contemporary mafic or intermediate igneous rocks, which would be expected if extensive fractional crystallization took place. Although the EM1-type mantle can generate Si-saturated shoshonitic syenite, the fractional crystallization of mafic minerals will occur in this process in order to generate syenite with depleted Fe, enriched Mg and Ca, significantly enriched Sr and Pb, and significant fractionation between LREE and HREE (Conceicão, Nardi, & Conceicão, 2000). These characteristics are significantly

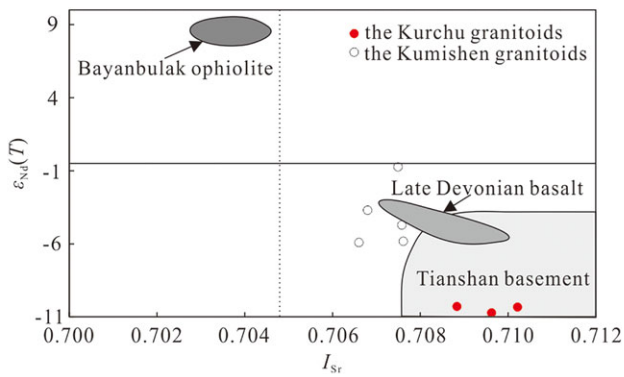

FIGURE 12 I_{Sr}–ε_{Nd}(T) diagram for the studied granodiorite. The Kumishen data are from Zhang et al. (2007), and other data are from Zhu, Cuo, Song, Zhan, and Gu (2009) [Colour figure can be viewed at wileyonlinelibrary.com]

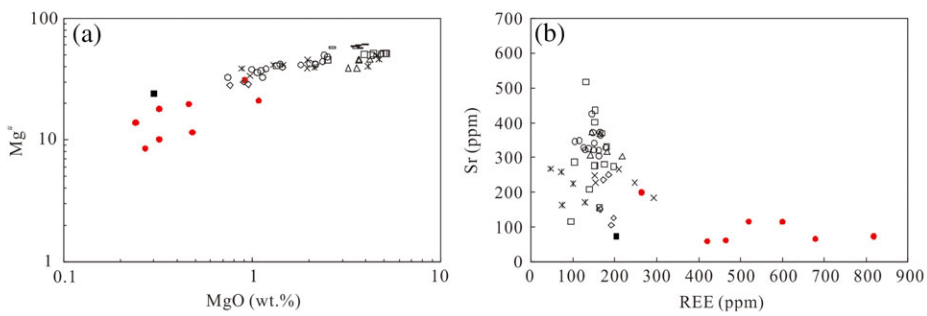

FIGURE 11 (a) MgO–Mg# diagram and (b) REE–Sr diagram for the studied PAG. The legend is the same as that in Figure 6 [Colour figure can be viewed at wileyonlinelibrary.com]

different from those of the Kurchu PAG. In addition, the trace element and isotopic compositions of magmas that are derived from the partial melting of the mantle have significant characteristics. The Nd/Th, Ti/Zr, and Ti/Y ratios of rock derived from the partial melting of the mantle are >15 (Bea, Arzamastsev, Montero, & Arzamastseva, 2001), >30 (Wedepohl, 1995), and >200 (Hergt, Peate, & Hawkesworth, 1991), respectively. However, the ratio of Nd/Th, Ti/Zr, and Ti/Y of the Kurchu PAG is <4.1, < 5.3, and <101.9 (except for two samples with values of 285 and 302), respectively. In addition, the rocks derived from the partial melting of the mantle may have low $(^{87}Sr/^{86}Sr)_i$ and high $\varepsilon_{Nd}(T)$ values. In contrast, the Kurchu PAG has high $(^{87}Sr/^{86}Sr)_i$ and lower negative $\varepsilon_{Nd}(T)$ values (Figure 12). Overall, a mantle source of the Kurchu PAG may be ruled out based on these results.

The potassic granites could also have resulted from the interaction of mantle-derived mafic melts with crustal material during the assimilation-fractional crystallization process (Zhou, Zhai, Zhao, Lan, & Sun, 2014). The rocks studied here are highly potassic, with limited variations in their major and trace element compositions. Although they have obvious depletions of Ba, Sr, Nb, Ta, and Eu, with low Sr/Y ratios (2.01–9.59), possibly suggesting that a certain degree of fractional crystallization did take place, an assimilation or magma mixing model can certainly account for the high K_2O contents of the potassic granites. However, this model fails to account for the low Sr levels of the granite (Zhou et al., 2014).

The studied rocks have enriched LREE patterns with negative Eu, Sr, Nb, and Ta anomalies and positive Zr and Hf anomalies, which are typical of a crustal source. In addition, the whole-rock isotopic data from the Kurchu PAG show high initial $^{87}Sr/^{86}Sr$ (0.712151–0.715436) and low ε_{Nd} (*T*) values. Together with Nd model ages (t_{DM2} = 1.99–2.02 Ga) that are much older than crystallization ages (418 Ma), these data indicate crustal contributions. Generally, Sr reflects the source composition, a small degree of melting or the fractionation/accumulation of plagioclase. The Y and Yb contents are controlled by garnet (Conly, Brenan, Bellon, & Scott, 2005). Because the mineral-melt partition coefficients are >1 for Sr in plagioclase and Y and Yb for amphibole/garnet, the low Sr/Y values, high Yb contents, and negative Eu anomalies of these rocks indicate that plagioclase could have been present and amphibole and garnet absent in the residual source (Watkins, Clemens, & Treloar, 2007). On the other hand, the studied rocks have significantly low CaO contents. Therefore, we favour that Ca-enriched plagioclase was present in the residue and that amphibole and garnet were absent in the residual source. In addition, the studied rocks are enriched in alkaline and $K_2O > Na_2O$, indicating that the source is enriched in K_2O. Therefore, the source cannot be amphibolite (Rapp, Watson, & Miller, 1991) or meta-basalt (Rapp & Watson, 1995), which would generate a magma that is enriched in Na_2O and depleted in K_2O. Overall, the source of the Kurchu PAG is derived from the partial melting of the K_2O-rich lower crust.

Previous studies have indicated that the sources of contemporaneous granitoids in the south margin of the Tarim Craton vary. For example, the Tiereke, Kurla, and Tiemenguan plutons were predominantly derived from the partial melting of the Palaeoproterozoic continental crust with inputs from juvenile depleted mantle materials (Ge et al., 2012; Guo et al., 2013). The Oxidaban and Bositen Lake plutons were generated by the partial melting of high-K meta-basalt (Guo et al., 2013). The Kumishen pluton was formed by the partial melting of Mesoproterozoic mantle-derived basic materials (Zhang et al., 2007). Obviously, the sources of contemporaneous granitoids in the south margin of the Tarim Craton are different from those of the Kurchu PAG.

6.3 | Tectonic setting and implications

Previous studies proposed that the Early Palaeozoic granitoids in the south margin of the Tarim Craton probably formed in an Andean-type continental arc (Ge et al., 2012; Guo et al., 2013; Zhang et al., 2007; Zhang et al., 2014; Zhu et al., 2008). However, the Kurchu PAGs have different geochemical characteristics, sources, and diagenetic conditions from the other granitoids in this area. Therefore, the tectonic setting of the Kurchu PAG may be different from those of the other granitoids. Recent geochronology and geochemical studies of granitoids in the south margin of the Tarim Craton have suggested that these granitoids were products of the southward subduction of the nearby South Tianshan Ocean under the Tarim Craton (Ge et al., 2012; Guo et al., 2013; Zhang et al., 2007; Zhang et al., 2014; Zhu et al., 2008) and that they were produced in the normal island arc of the active continental margin. Generally, a compressional tectonic setting occurs in the island arc of the active continental margin, and granites produced in this tectonic setting have high water contents and oxygen fugacity due to the subduction of oceanic crust, which can generate much more H_2O from its hydrous minerals (Grove, Till, & Krawczynski, 2015). As H_2O acts as an efficient oxidizing agent in magma and the mantle (Brandon & Draper, 1998; Parkinson & Arculus, 1999; Wood et al., 1990), the magma in the island arc of the active continental margin has high oxygen fugacity. However, the Kurchu PAG has a lower water content and oxygen fugacity, so those PAGs may not be generated in the island arc of the active continental margin. We favour that the Kurchu PAGs were generated in a back-arc environment: (a) there are many Early Palaeozoic sedimentary strata occurring in surrounding area of the Kurchu, such as the Arpishenmaibulake Formation in north-eastern margin of the Tarim Craton and the Keziertake Formation in north-western margin of the Tarim Craton; (b) in the Q–A–P (Figure 6b) and SiO_2–FeO_t/(FeO_t + MgO) diagrams (Figure 13), the samples plot in the continental epeirogenic uplift granitoid area, indicating that the Kurchu PAG formed in an extensional environment; (c) the lower water content and oxygen fugacity of the Kurchu PAG indicate that the source of this rock may be less affected by the subduction, therefore indicating that the source of the Kurchu PAG was located far from the active continental margin; (d) the lower diagenetic pressure and less shallow emplacement depth of the Kurchu PAG indicate that the source of this rock should be in an extensional environment where the continental crustal is thin. In a subduction system, a back-arc basin is the place that occurs as an extensional environment and has relatively thin crust (Liu, Wang, & Chen, 2017); (e) the Kurchu PAG has a high crystallization temperature, indicating that there is sufficient heat for the partial melting of the crust. Generally, upwelling and the decompression melting of the asthenosphere, which induce basaltic magma to underplate the lower crust, occur in back-arc environments. There

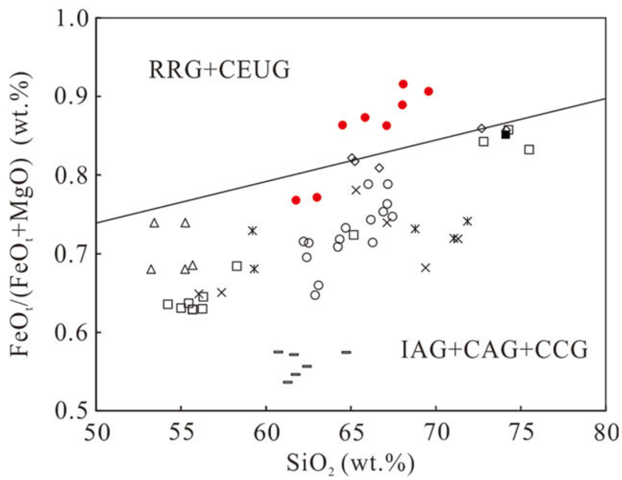

FIGURE 13 $FeO_t/(FeO_t + MgO)–SiO_2$ diagram for the studied granodiorite, after Maniar and Piccoli (1989). The legend is the same as that in Figure 6 [Colour figure can be viewed at wileyonlinelibrary.com]

was an approximately 1,200-km-long, nearly E–W-trending magmatic belt along the northern margin of the Tarim block, which concentrically occurred in 418–420 Ma (Figure 2). This magmatic "flare-up" in the Northern Tarim block was also triggered by asthenospheric upwelling. Therefore, a back-arc basin is a suitable environment for the Kurchu PAG; (f) Han et al. (2004) found Early Palaeozoic (380–490 Ma) A-type granites in this area, thus also indicating that this region may have been an extensional environment during the Early Palaeozoic.

As previously mentioned, two conflicting dynamic models have been proposed to explain the subduction polarity of the South Tianshan. The northward subduction model was proposed (Allen et al., 1993; Chen, Lu, Jia, Cai, & Wu, 1999; Gao et al., 1998; Windley et al., 1990; Xiao et al., 2004; Xiao et al., 2009) based on the widespread arc magmatism in the KYB and the CTB and the occurrence of HP–UHP metamorphic rocks along the southern CTB. This model interprets the northern Tarim Craton as passive margin sediments. In contrast, the southward subduction model was proposed (Charvet et al., 2011; Lin et al., 2009; Wang et al., 2010) mainly based on the "top to the north" ductile deformation in accretionary complexes and widespread arc magmatism in the northern Tarim Craton, which has been interpreted as an active continental margin (Ge et al., 2012; Guo et al., 2013; Zhang et al., 2007; Zhang et al., 2014; Zhu et al., 2008). One of the focuses of this disagreement is whether the Palaeozoic northern margin of the Tarim Craton is passive or active. The previous identification of the Silurian (ca. 420 Ma) arc granitoids in this area strongly favours that the northern Tarim Craton was an active margin during the Early Palaeozoic, or it must have changed into an active margin with arc magmatism by at least ca. 420 Ma (e.g., Ge et al., 2012; Guo et al., 2013; Zhang et al., 2007; Zhang et al., 2014; Zhu et al., 2008). However, the Cambrian–Ordovician and Carboniferous marine carbonate sequences and the fact that few volcanics have been found in these sequences may strongly argue against this interpretation (e.g., Carroll, 1995; Carroll, Graham, Chang, & Mcknight, 2001; Chen et al., 1999). Fortunately, our identification of the Silurian back-arc granitoids in the Kurchu area can provide an interpretation for these conflicts. As some regions, such as Kurchu, Yeyungou, and Bayanbulak, of the northern margin of the Tarim Craton represented a back-arc basin during the Early Palaeozoic, sedimentary rocks would have formed after the Early Palaeozoic, such as the Carboniferous marine carbonate sequences. These sedimentary rocks would have overlain most Early Palaeozoic rocks, leading to the few volcanics that have been found in this area. In addition, the back-arc granitoids presented here clearly intrude the basement of the Tarim Craton. This back-arc magmatism can be interpreted by the southward subduction of the South Tianshan Ocean. Therefore, the Kurchu PAGs not only provide strong evidence that the Palaeozoic northern margin of the Tarim Craton is active but also structure a complete southward subduction system of the South Tianshan Ocean. In addition, this interpretation implies that the southward subduction of the South Tianshan Ocean must have been initiated well before ca. 420 Ma, as the back-arc basin had developed in the subduction system.

7 | CONCLUSIONS

A late Early Palaeozoic (ca. 418 Ma) magmatism event occurred in the northern Tarim Craton. The magma has the geochemical characteristics of high K_2O, alkali ($K_2O + Na_2O$), REE, Zr, and Hf concentrations and low MgO, Cao, and Sr concentrations. The magma was probably derived from the partial melting of the Palaeoproterozoic continental crust at high temperatures, low pressure, and anhydrous and low oxygen fugacity conditions and emplaced at shallow depths. This magmatic event likely occurred in a back-arc environment, which implies that the northern Tarim Craton was an active continental margin in the Early Palaeozoic and that the subduction of the Southern Tianshan Ocean was initiated well before ca. 418 Ma.

ACKNOWLEDGEMENTS

This study was financially supported by the National 305 Project (2011BAB06B02-03) and the Deep Resources Exploration and Mining, a Special Project in the Framework of National Key R&D Program of China (2017YFC0602302). We are grateful to a number of technical staff members for their assistance during this study. We also thank Professor Christina Yan Wang, Dr. Mengxi Wang, and Master Chunmei Ma for their help. Comments and suggestions from the journal's anonymous reviewers greatly improved the quality of this work.

ORCID

Rui Liu https://orcid.org/0000-0001-7800-5504

REFERENCES

Abbasi, S., Manesh, S. M. T., Karimi, S., & Parfenova, O. V. (2014). Relative contributions of crust and mantle to generation of Oligo-Miocene medium-K calc-alkaline I-type granitoids in a subduction setting—A case study from the Nabar Pluton, central Iran. *Petrology*, *22*(3), 310–328.

Allen, M. B., Windley, B. F., & Zhang, C. (1993). Palaeozoic collisional tectonics and magmatism of the Chinese Tien Shan, central Asia. *Tectonophysics*, *220*(1–4), 89–115.

Aoki, K., Ishiwaka, K., & Kanisawa, S. (1981). Fluorine geochemistry of basaltic rocks from continental and oceanic regions and petrogenetic application. *Contributions to Mineralogy & Petrology*, *76*, 53–59.

Arculus, R. J., & Johnson, R. W. (1978). Criticism of generalised models for the magmatic evolution of arc-trench systems. *Earth & Planetary Science Letters*, *39*(1), 118–126.

Baker, D. R., Conte, A. M., Freda, C., & Ottolini, L. (2002). The effect of halogens on Zr diffusion and zircon dissolution in hydrous metaluminous granitic melts. *Contributions to Mineralogy & Petrology*, *142*(6), 666–678. https://doi.org/10.1007/s00410-001-0328-3

Barley, M. E., Eisenlohr, B. N., Groves, D. I., Perring, C. S., & Vearncombe, J. R. (1989). Late Archean convergent margin tectonics and gold mineralization: A new look at the Norseman-Wiluna Belt, Western Australia. *Geology*, *17*(9), 826–829. https://doi.org/10.1130/0091-7613(1989)017<0826:LACMTA>2.3.CO;2

Bea, F., Arzamastsev, A., Montero, P., & Arzamastseva, L. (2001). Anomalous alkaline rocks of Soustov, Kola: Evidence of mantle-derived metasomatic fluids affecting crustal materials. *Contributions to Mineralogy & Petrology*, *140*(5), 554–566. https://doi.org/10.1007/s004100000211

Brandon, A. D., & Draper, D. S. (1998). Reply to the comment by B. R. Frost and C. Ballhaus on "Constraints on the origin of the oxidation state of mantle overlying subduction zones: An example from Simcoe, Washington, USA". *Geochim et Cosmochim Acta*, *62*, 333–335.

Brooks, C., Ludden, J., Pigeon, J. Y., & Hubregtse, J. M. W. (1982). Volcanism of shoshonite to high-K andesite affinity in an Archean are environment, Oxford Lake, Manitoba. *Canadian Journal of Earth Sciences*, *19*(1), 55–67. https://doi.org/10.1139/e82-005

Bucholz, C. E., Jagoutz, O., Schmidt, M. W., & Sambuu, O. (2014). Fractional crystallization of high-K arc magmas: Biotite- versus amphibole-dominated fractionation series in the Dariv Igneous Complex, Western Mongolia. *Contributions to Mineralogy & Petrology*, *168*(5), 1072. https://doi.org/10.1007/s00410-014-1072-9

Campbell, I. H., Stepanov, A. S., Liang, H. Y., Allen, C. M., Norman, M. D., Zhang, Y. Q., & Xie, Y. W. (2014). The origin of shoshonites: New insights from the Tertiary high-potassium intrusions of eastern Tibet. *Contributions to Mineralogy & Petrology*, *167*(3), 983. https://doi.org/10.1007/s00410-014-0983-9

Carr, P. F. (1998). Subduction-related Late Permian shoshonites of the Sydney Basin, Australia. *Mineralogy & Petrology*, *63*(1–2), 49–71. https://doi.org/10.1007/BF01162768

Carroll, A. R. (1995). Late Paleozoic tectonic amalgamation of northwestern China: Sedimentary record of the northern Tarim, northwestern Turpan, and southern Junggar Basins. *Geological Society of America Bulletin*, *107*(5), 571–594. https://doi.org/10.1130/0016-7606(1995)107<0571:LPTAON>2.3.CO;2

Carroll, A. R., Graham, S. A., Chang, E. Z., & Mcknight, C. (2001). Sinian through Permian tectonostratigraphic evolution of the northwestern Tarim Basin, China. *Geological Society of America Memoirs*, *194*, 47–69.

Charvet, J., Shu, L. S., Laurent-Charvet, S., Wang, B., Faure, M., Cluzel, D., & Jong, K. D. (2011). Palaeozoic tectonic evolution of the Tianshan Belt, NW China. *Science China Earth Sciences*, *54*(2), 166–184. https://doi.org/10.1007/s11430-010-4138-1

Chen, C., Lu, H., Jia, D., Cai, D., & Wu, S. (1999). Closing history of the southern Tianshan Oceanic Basin, western China: An oblique collisional orogeny. *Tectonophysics*, *302*(1–2), 23–40. https://doi.org/10.1016/S0040-1951(98)00273-X

Chen, Y. J., Chen, H. Y., Zaw, K., Pirajno, F., & Zhang, Z. J. (2004). The geodynamic setting of large-scale metallogenisis in mainland China, exemplified by skarn type gold deposits. *Earth Science Froniters*, *11*(4), 57–83. (in Chinese with English abstract)

Clemens, J. D., & Vielzeuf, D. (1987). Constraints on melting and magma production in the crust. *Earth & Planetary Science Letters*, *86*(2), 287–306. https://doi.org/10.1016/0012-821X(87)90227-5

Conceicão, R. V., Nardi, L. V. S., & Conceicão, H. (2000). The SantanÃ¡polis Syenite: Genesis and evolution of Paleoproterozoic shoshonitic syenites in Northeastern Brazil. *International Geology Review*, *42*(10), 941–957. https://doi.org/10.1080/00206810009465119

Conly, A. G., Brenan, J. M., Bellon, H., & Scott, S. D. (2005). Arc to rift transitional volcanism in the Santa Rosalía Region, Baja California Sur, Mexico. *Journal of Volcanology and Geothermal Research*, *142*(3), 303–341. https://doi.org/10.1016/j.jvolgeores.2004.11.013

Costa, F. G., Oliveira, E. P., & McNaughton, N. J. (2011). The Fazenda Gavião granodiorite and associated potassic plutons as evidence for Palaeoproterozoic arc-continent collision in the Rio Itapicuru Greenstone Belt, Brazil. *Journal of South American Earth Sciences*, *32*(2), 127–141. https://doi.org/10.1016/j.jsames.2011.04.012

Ding, H., Zhang, Z., Dong, X., Yan, R., Lin, Y., & Jiang, H. (2015). Cambrian ultrapotassic rhyolites from the Lhasa Terrane, south Tibet: Evidence for Andean-type magmatism along the northern active margin of Gondwana. *Gondwana Research*, *27*(4), 1616–1629. https://doi.org/10.1016/j.gr.2014.02.003

Edgar, A. D., & Arima, M. (1985). Fluorine and chlorine contents of phlogopites crystallized from ultrapotassic rock compositions in high pressure experiments: Implication for halogen reservoirs in source regions. *American Mineralogist*, *213*(2), 97–108.

Ellam, R. M., & Hawkesworth, C. J. (1988). Elemental and isotopic variations in subduction related basalts: Evidence for a three component model. *Contributions to Mineralogy & Petrology*, *98*(1), 72–80. https://doi.org/10.1007/BF00371911

Foley, S., & Peccerillo, A. (1992). Potassic and ultrapotassic magmas and their origin. *Lithos*, *28*(3–6), 181–185. https://doi.org/10.1016/0024-4937(92)90005-J

Frost, B. R., Barnes, C. G., Collins, W. J., Arculus, R. J., Ellis, D. J., & Frost, C. D. (2001). A geochemical classification for granitic rocks. *Journal of Petrology*, *42*(11), 2033–2048. https://doi.org/10.1093/petrology/42.11.2033

Frost, C. D., Frost, B. R., Bell, J. M., & Chamberlain, K. R. (2002). The relationship between A-type granites and residual magmas from anorthosite: Evidence from the northern Sherman batholith, Laramie Mountains, Wyoming, USA. *Precambrian Research*, *119*(1), 45–71. https://doi.org/10.1016/S0301-9268(02)00117-1

Gao, J., & Klemd, R. (2003). Formation of HP–LT rocks and their tectonic implications in the western Tianshan Orogen, NW China: Geochemical and age constraints. *Lithos*, *66*(1), 1–22. https://doi.org/10.1016/S0024-4937(02)00153-6

Gao, J., Klemd, R., Qian, Q., Zhang, X., Li, J., Jiang, T., & Yang, Y. (2012). The collision between the Yili and Tarim blocks of the Southwestern Altaids: Geochemical and age constraints of a leucogranite dike crosscutting the HP–LT metamorphic belt in the Chinese Tianshan Orogen. *Tectonophysics*, *499*(1), 118–131.

Gao, J., Li, M., Xiao, X., Tang, Y., & He, G. (1998). Paleozoic tectonic evolution of the Tianshan Orogen, northwestern China. *Tectonophysics*, *287*(1–4), 213–231. https://doi.org/10.1016/S0040-1951(97)00211-4

Ge, R., Zhu, W., Wu, H., Zheng, B., Zhu, X., & He, J. (2012). The Paleozoic northern margin of the Tarim Craton: Passive or active? *Lithos*, *142-143*(6), 1–15. https://doi.org/10.1016/j.lithos.2012.02.010

Grove, T. L., Till, C. B., & Krawczynski, M. J. (2015). The role of H_2O in subduction zone magmatism. *Annual Review of Earth & Planetary Sciences*, *40*(1), 413–439.

Guo, R., Qin, Q., Zari, M., Zhao, L., Sun, M., & Wei, Z. (2013). Geological characteristics and tectonic significance of Ordovician granite intrusions in the western segment of Quruqtagh, Xinjiang. *Earth Science Frontiers*, *20*(4), 251–263. (in Chinese with English abstract)

Han, B. F., He, G. Q., & Wu, T. R. (2004). Zircon U-Pb dating and geochemical features of early Paleozoic granites from Tianshan, Xinjiang: Implications for tectonic evolution. *Xinjiang Geology*, *1*, 1–8. (in Chinese with English abstract)

Hari, K. R., Chalapathi, N. V., Vikas, S., & Guiting, H. (2014). Alkali feldspar syenites with shoshonitic affinities from Chhotaudepur area: Implication for mantle metasomatism in the Deccan large igneous province. *Geoscience Frontiers*, *5*(2), 261–276. https://doi.org/10.1016/j.gsf.2013.06.007

Hergt, J. M., Peate, D. W., & Hawkesworth, C. J. (1991). The petrogenesis of Mesezoic Gondwana low-Ti flood basalts. *Earth & Planetary Science Letters*, *105*(1–3), 134–148. https://doi.org/10.1016/0012-821X(91)90126-3

Holtz, F. (1992). Effects of H_2O on liquidus phase relations in the haplogranite system at 2 and 5 kbar. *American Mineralogist*, *77*(11), 1223–1241.

Hoskin, P. W. O., & Schaltegger, U. (2003). The composition of zircon and igneous and metamorphic petrogenesis. *Rev.miner.geochem*, \(1), 27–62.

Jahn, B. M. (2004). The Central Asian Orogenic Belt and growth of the continental crust in the Phanerozoic. *Aspects of the Tectonic Evolution of China*, *226*(1), 73–100.

Jiang, Y. H., Jiang, S. Y., Ling, H. F., Zhou, X. R., Rui, X. J., & Yang, W. Z. (2002). Petrology and geochemistry of shoshonitic plutons from the western Kunlun Orogenic Belt, Xinjiang, northwestern China: Implications for granitoid geneses. *Lithos*, *63*(3–4), 165–187. https://doi.org/10.1016/S0024-4937(02)00140-8

Jiang, Y. H., Wang, G. C., Liu, Z., Ni, C. Y., Long, Q., & Zhang, Q. (2015). Repeated slab advance-retreat of the Palaeo-Pacific plate underneath SE China. *International Geology Review*, *57*(4), 472–491. https://doi.org/10.1080/00206814.2015.1017775

Küster, D., & Harms, U. (1998). Post-collisional potassic granitoids from the southern and northwestern parts of the Late Neoproterozoic East African Orogen: A review. *Lithos*, *45*(1–4), 177–195. https://doi.org/10.1016/S0024-4937(98)00031-0

Li, H., Ling, M. X., Li, C. Y., Zhang, H., Ding, X., Yang, X. Y., & Sun, W. D. (2012). A-type granite belts of two chemical subgroups in central eastern China: Indication of ridge subduction. *Lithos*, *150*(10), 26–36. https://doi.org/10.1016/j.lithos.2011.09.021

Lin, W., Faure, M., Shi, Y., Wang, Q., & Li, Z. (2009). Palaeozoic tectonics of the south-western Chinese Tianshan: New insights from a structural study of the high-pressure/low-temperature metamorphic belt. *International Journal of Earth Sciences*, *98*(6), 1259–1274. https://doi.org/10.1007/s00531-008-0371-7

Liu, D., Zhao, Z., Zhu, D. C., Niu, Y., Depaolo, D. J., Harrison, T. M., & Sun, C. (2014). Postcollisional potassic and ultrapotassic rocks in southern Tibet: Mantle and crustal origins in response to India–Asia collision and convergence. *Geochimica et Cosmochimica Acta*, *143*(27), 207–231. https://doi.org/10.1016/j.gca.2014.03.031

Liu, R., Wang, L. X., & Chen, G. W. (2017). Genesis,geological significance and metallogentic potentiality of A-type granites in the Awulale area of the western Tianshan, Xinjiang. *Acta Petrologica Sinica*, *33*(6), 1741–1754.

Liu, Z., Jiang, Y. H., Jia, R. Y., Zhao, P., & Zhou, Q. (2015). Origin of Late Triassic high-K calc-alkaline granitoids and their potassic microgranular enclaves from the western Tibet Plateau, northwest China: Implications for Paleo-Tethys evolution. *Gondwana Research*, *27*(1), 326–341. https://doi.org/10.1016/j.gr.2013.09.022

Lu, S., Li, H., Zhang, C., & Niu, G. (2008). Geological and geochronological evidence for the Precambrian evolution of the Tarim Craton and surrounding continental fragments. *Precambrian Research*, *160*(1), 94–107. https://doi.org/10.1016/j.precamres.2007.04.025

Ludwig, K. R. (2000). *Users manual for ISOPLOT/EX, version 2. A geochronological toolkit for Microsoft Excel*. Berkeley: Berkeley Geochronology Center Special Publication.

Mallik, A., Nelson, J., & Dasgupta, R. (2015). Partial melting of fertile peridotite fluxed by hydrous rhyolitic melt at 2–3 GPa: Implications for mantle wedge hybridization by sediment melt and generation of ultrapotassic magmas in convergent margins. *Contributions to Mineralogy & Petrology*, *169*(5), 48. https://doi.org/10.1007/s00410-015-1139-2

Maniar, P., & Piccoli, P. (1989). Tectonic discrimination of granitoids. *Geological Society of America Bulletin*, *101*, 635–643. https://doi.org/10.1130/0016-7606(1989)101<0635:TDOG>2.3.CO;2

Miller, C., Schuster, R., Klötzli, U., Frank, W., & Purtscheller, F. (1999). Post-collisional potassic and ultrapotassic magmatism in SW Tibet: Geochemical and Sr–Nd–Pb–O isotopic constraints for mantle source characteristics and petrogenesis. *Journal of Petrology*, *40*(9), 699–715.

Morrison, G. W. (1980). Characteristics and tectonic setting of the shoshonite rock association. *Lithos*, *13*(1), 97–108. https://doi.org/10.1016/0024-4937(80)90067-5

Nabatian, G., Ghaderi, M., Neubauer, F., Honarmand, M., Liu, X., Dong, Y., & Bernroider, M. (2014). Petrogenesis of Tarom high-potassic granitoids in the Alborz–Azarbaijan Belt, Iran: Geochemical, U–Pb zircon and Sr–Nd–Pb isotopic constraints. *Lithos*, *184-187*(1), 324–345. https://doi.org/10.1016/j.lithos.2013.11.002

Orozco-Garza, A., Dostal, J., Keppie, J. D., & Paz-Moreno, F. A. (2013). Mid-tertiary (25–21 Ma) lamprophyres in NW Mexico derived from subduction-modified subcontinental lithospheric mantle in an extensional backarc environment following steepening of the Benioff zone. *Tectonophysics*, *590*(2), 59–71. https://doi.org/10.1016/j.tecto.2013.01.013

Parkinson, I. J., & Arculus, R. J. (1999). The redox state of subduction zones: Insights from arc-peridotites. *Chemical Geology*, *160*(4), 409–423. https://doi.org/10.1016/S0009-2541(99)00110-2

Patiňo-Douce, A. E., & McCarty, T. C. (1998). Melting of crustal rocks during continetal collision and subduction. *Springer Netherlands*, *10*, 27–55.

Peccerillo, A. (1992). Potassic and ultrapotassic rocks: Compositional characteristics, petrogenesis, and geologic significance. *Episodes*, *15*(4), 243–251.

Peccerillo, A., & Taylor, T. S. (1976). Geochemistry of Eocene calc-alkaline volcanic rocks form Kastamonu area, Northern Turkey. *Contributions to Mineralogy and Petrology*, *56*(1), 63–81.

Rao, N. V. C., Srivastava, R. K., Sinha, A. K., & Ravikant, V. (2014). Petrogenesis of Kerguelen mantle plume-linked Early Cretaceous ultrapotassic intrusive rocks from the Gondwana sedimentary basins, Damodar Valley, Eastern India. *Earth-Science Reviews*, *136*(3), 96–120.

Rapp, R. P., & Watson, E. B. (1995). Dehydration melting of metabasalt at 8–32 kbar: Implications for continental growth and crust-mantle recycling. *Journal of Petrology*, *36*(4), 891–931. https://doi.org/10.1093/petrology/36.4.891

Rapp, R. P., Watson, E. B., & Miller, C. F. (1991). Partial melting of amphibolite/eclogite and the origin of Archean trondhjemites and tonalites. *Precambrian Research*, *51*(1–4), 1–25. https://doi.org/10.1016/0301-9268(91)90092-O

Richards, J. (2005). Cumulative factors in the generation of giant calc-alkaline porphyry Cu deposits. In T. M. Porter (Ed.), *Super porphyry copper & gold deposits* (pp. 1B7–1B25). Toronto: PGC Publishing.

Rios, D. C., Conceição, H., Davis, D. W., Cid, J. P., Rosa, M. L. S., Macambira, M. J. B., & Davis, W. J. (2007). Paleoproterozoic potassic–ultrapotassic magmatism: Morro do Afonso Syenite Pluton, Bahia, Brazil. *Precambrian Research*, *154*(1), 1–30. https://doi.org/10.1016/j.precamres.2006.11.015

Roberts, M. P. (1993). Origin of high-potassium, calc-alkaline, I-type granitoids. *Geology*, *21*(9), 825. https://doi.org/10.1130/0091-7613(1993)021<0825:OOHPTA>2.3.CO;2

Rogers, N. W., Hawkesworth, C. J., Parker, R. J., & Marsh, J. S. (1985). The geochemistry of potassic lavas from Vulsini, central Italy and implications for mantle enrichment processes beneath the Roman region. *Contributions to Mineralogy & Petrology*, *90*(2–3), 244–257. https://doi.org/10.1007/BF00378265

Saunders, A. D., Tarney, J., & Weaver, S. D. (1980). Transverse geochemical variations across the Antarctic Peninsula: Implications for the genesis of calc-alkaline magmas. *Earth & Planetary Science Letters*, *46*(3), 344–360. https://doi.org/10.1016/0012-821X(80)90050-3

Shand, S. J. (1943). *The eruptive rocks* (2nd ed.). New York: John Wiley.

Shen, P., Shen, Y. C., Liu, T. B., Li, G. M., & Zeng, Q. D. (2008). Geology and geochemistry of the Early Carboniferous Eastern Sawur caldera complex and associated gold epithermal mineralization, Sawur Mountains, Xinjiang, China. *Journal of Asian Earth Sciences*, *32*(2), 259–279. https://doi.org/10.1016/j.jseaes.2007.10.004

Sun, S. S., & McDonough, W. (1989). Chemical and isotopic systematics of ocean basalts: Implications for mantle composition and processes, in Magmatism in the Ocean Basins. *Geological Society London Special Publications*, *42*, 313–345. https://doi.org/10.1144/GSL.SP.1989.042.01.19

Sun, W. D., Huang, R. H., Li, H., Hu, Y. B., Zhang, C. C., Sun, S. J., & Ling, M. X. (2015). Porphyry deposits and oxidized magmas. *Ore Geological Reviews*, *65*(1), 97–131. https://doi.org/10.1016/j.oregeorev.2014.09.004

Sverjensky, D. A. (1984). Europium redox equilibria in aqueous solution. *Earth & Planetary Science Letters*, *67*(1), 70–78. https://doi.org/10.1016/0012-821X(84)90039-6

Torabi, G. (2011). Middle Eocene volcanic shoshonites from western margin of Central-East Iranian Microcontinent (CEIM), a mark of previously subducted CEIM-confining oceanic crust. *Petrology*, *19*(7), 675–689. https://doi.org/10.1134/S0869591111030039

Turner, S. P., Foden, J. D., & Morrison, R. S. (1992). Derivation of some A-type magmas by fractionation of basaltic magma: An example from Padthway Ridge. *Lithos*, *28*(2), 151–179. https://doi.org/10.1016/0024-4937(92)90029-X

Wang, B., Faure, M., Shu, L., Jong, K. D., Charvet, J., Cluzel, D., & Ruffet, G. (2010). Structural and geochronological study of high-pressure metamorphic rocks in the Kekesu section (Northwestern China): Implications for the late Paleozoic tectonics of the Southern Tianshan. *Journal of Geology*, *118*(1), 59–77. https://doi.org/10.1086/648531

Watkins, J. M., Clemens, J. D., & Treloar, P. J. (2007). Archaean TTGs as sources of younger granitic magmas: Melting of sodic metatonalites at 0.6–1.2 GPa. *Contributions to Mineralogy & Petrology*, *154*(1), 91–110. https://doi.org/10.1007/s00410-007-0181-0

Watson, E. B., & Harrison, T. M. (1983). Zircon saturation revisited: Temperature and composition effects in a variety of crustal magma types. *Earth & Planetary Science Letters*, *64*(2), 295–304. https://doi.org/10.1016/0012-821X(83)90211-X

Wedepohl, K. H. (1995). The composition of the continental crust. *Geochimica et Cosmochim Acta*, *59*, 1217–1232. https://doi.org/10.1016/0016-7037(95)00038-2

Whitney, J. A. (1975). Vapor generation in a quartz monzonite magma: A synthetic model with application to prophyry copper deposits. *Economic Geology*, *70*(2), 346–358. https://doi.org/10.2113/gsecongeo.70.2.346

Windley, B. F., Allen, M. B., Zhang, C., Zhao, Z. Y., & Wang, G. R. (1990). Paleozoic accretion and Cenozoic redeformation of the Chinese Tien Shan Range, central Asia. *Geology*, *18*(2), 128. https://doi.org/10.1130/0091-7613(1990)018<0128:PAACRO>2.3.CO;2

Wood, B. J., Bryndzia, L. T., & Johnson, K. E. (1990). Mantle oxidation state and its relationship to tectonic environment and fluid speciation. *Science*, *248*(4953), 337–345. https://doi.org/10.1126/science.248.4953.337

Woodhead, J. D., Hergt, J. M., Davidson, J. P., & Eggins, S. M. (2001). Hafnium isotope evidence for 'conservative' element mobility during subduction zone processes. *Earth & Planetary Science Letters*, *192*(3), 331–346. https://doi.org/10.1016/S0012-821X(01)00453-8

Wyllie, P. J., & Sekine, T. (1982). The formation of mantle phlogopite in subduction zone hybridization. *Contributions to Mineralogy & Petrology*, *79*(4), 375–380. https://doi.org/10.1007/BF01132067

Wyman, D. A., & Kerrich, R. (1989). Archean lamprophyre dikes of the Superior Province, Canada: Distribution, petrology, and geochemical characteristics. *Journal of Geophysical Research Solid Earth*, *94*(B4), 4667–4696. https://doi.org/10.1029/JB094iB04p04667

XBGMR. (1993). *Regional Geology of Xinjiang Uygur Autonomy Region*. Beijing: Geological Publishing House.

Xiao, W., Zhang, L. C., Qin, K. Z., Sun, S., & Li, J. L. (2004). Paleozoic accretionary and collisional tectonics of the Eastern Tianshan (China): Implications for the continental growth of central Asian. *Amercian Journal of Science*, *304*, 370–395. https://doi.org/10.2475/ajs.304.4.370

Xiao, W. J., Windley, B. F., Huang, B. C., Han, C. M., Yuan, C., Chen, H. L., & Li, J. L. (2009). End-Permian to mid-Triassic termination of the accretionary processes of the southern Altaids: Implications for the geodynamic evolution, Phanerozoic continental growth, and metallogeny of Central Asia. *International Journal of Earth Sciences*, *98*(6), 1189–1217. https://doi.org/10.1007/s00531-008-0407-z

Yang, W. B., Niu, H. C., Shan, Q., Luo, Y., Sun, W. D., Li, C. Y., .Yu, X. Y. (2012). Late Paleozoic calc-alkaline to shoshonitic magmatism and its geodynamic implications, Yuximolegai area, western Tianshan, Xinjiang. *Gondwana Research*, *22*(1), 325–340, https://doi.org/10.1016/j.gr.2011.10.008.

Yardley, B. W. D., & Valley, J. W. (1997). The petrologic case for a dry lower crust. *Journal of Geophysical Research Solid Earth*, *102*(B6), 12173–12185. https://doi.org/10.1029/97JB00508

Zhang, B., Chen, W., Shun, Y. U., Yin, J. Y., Jie, L. I., Sun, J. B., & Yang, J. (2014). Subduction process of South Tianshan Ocean during Paleozoic. *Acta Petrologica Sinica*, *30*(8), 2351–2362. (in Chinese with English abstract)

Zhang, C. L., Zhou, D. W., Wang, J. L., & Wang, R. S. W. (2007). Geochronology,geochemistry and Sr–Nd isotopic composition and genesis implications of Huangjianshishan granite intrusion in Kumishi area of southern Tianshan. *Acta Petrologica Sinica*, *23*(8), 1821–1829. (in Chinese with English abstract)

Zhou, Y., Zhai, M., Zhao, T., Lan, Z., & Sun, Q. (2014). Geochronological and geochemical constraints on the petrogenesis of the early Paleoproterozoic potassic granite in the Lushan area, southern margin of the North China Craton. *Journal of Asian Earth Sciences*, *94*, 190–204. https://doi.org/10.1016/j.jseaes.2014.03.003

Zhu, W., Charvet, J., Xiao, W., & Jahn, B. M. (2011). Continental accretion and intra-continental deformation of the Central Asian Orogenic Belt. *Journal of Asian Earth Sciences*, *42*(5), 769–773. https://doi.org/10.1016/j.jseaes.2011.07.021

Zhu, Y. F., Cuo, X., Song, B., Zhan, L. R., & Gu, L. B. (2009). Petrology, Sr-Nd-Hf isotopic geochemistry and zircon chronology of the Late Palaeozoic volcanic rocks in the southwestern Tianshan Mountains, Xinjiang, NW China. *Journal of the Geological Society*, *166*(6), 1085–1099.

Zhu, Z. X., Li, J. Y., Dong, L. H., Wang, K. Z., Liu, G. Z., Li, Y. P., & Liu, Z. T. (2008). Age determination and geological significance of Devonian granitic intrusions in Seriyakeyilake region, northern margin of Tarim Basin, Xinjiang. *Acta Petrologica Sinica*, *24*(5), 971–976. (in Chinese with English abstract)

How to cite this article: Chen G, Yang J, Liu R. Potassic alkaline granitoid magmatism in the northern margin of the Tarim Craton: First evidence of a back-arc extensional environment. *Geological Journal*. 2020;55:771–785. https://doi.org/10.1002/gj.3450